Journal of Power Sources 195 (2010) 7600–7608

Contents lists available at ScienceDirect

Journal of Power Sources

journal homepage: www.elsevier.com/locate/jpowsour

Potential suitability of ferritic and austenitic steels as interconnect materials for solid oxide fuel cells operating at 600 °C

L. Niewolak*, E. Wessel, L. Singheiser, W.J. Quadakkers*

Forschungszentrum Jülich, Institute of Energy Research (IEF-2), 52425 Jülich, FRG, Germany

ARTICLE INFO

Article history:
Received 12 February 2010
Received in revised form 26 May 2010
Accepted 2 June 2010
Available online 9 June 2010

Keywords:
SOFC
Interconnect
Ferritic steel
σ-Phase
Oxidation

ABSTRACT

The oxidation behavior of a number of commercially available ferritic and austenitic steels was tested in air and in two simulated anode gases of a solid oxide fuel cell (SOFC) to evaluate the potential suitability as construction materials for interconnects in SOFC's operating at 600 °C. During air exposure all studied materials showed excellent oxidation resistance due to formation of a protective, double layered chromia/spinel surface scale even if the steel Cr content was as low as 17%. However, in the anode side gases the presence of water vapour (and possibly CO/CO_2) increased the tendency to form poorly protective Fe-base oxide scales, in combination with internal oxidation of Cr. The occurrence of this adverse effect could be suppressed not only by increased Cr contents of the alloy but also by a small alloy grain size either in the bulk of the material or in the specimen/component surface. The latter can be promoted by cold work e.g. introduced by specimen/component grinding. As high Cr contents may lead to undesired σ-phase formation and defined surface treatments of an interconnect will not be possible in all designs, the relatively low operating temperature of 600 °C, resulting in low Cr diffusivity in the alloy grains, may require the use of a fine grained interconnect material to obtain and sustain protective chromia base surface scale formation during long-term operation.

1. Introduction

A solid oxide fuel cell (SOFC) is an electrochemical device that converts the chemical energy in fuels into electrical energy by utilizing the natural tendency of oxygen and hydrogen to react [1]. Compared to other fuel cell systems a main advantage of the SOFC is its ability to use not only hydrogen but also presently available fossil fuels (such as methane, butane or even reformed gasoline and diesel), thus reducing operating costs and flexibility. In an SOFC system the single cell is constructed with an electrolyte (e.g. yttria stabilized zirconia-YSZ) arranged between a porous anode (e.g. Ni/ZrO_2-cermet) and cathode (e.g. $(La,Sr)MnO_3$) [2–4]. In anode substrate supported planar SOFC designs the components are assembled in flat stacks, with air and fuel flowing through channels commonly built into the so called metallic interconnects. In an SOFC stack the metallic interconnect thus provides the separation of the gas atmospheres, the electrical connection between the various single cells and acts as current collector [5–9].

The most commonly used construction materials for SOFC interconnects operating at temperatures around 800 °C are high-Cr ferritic steels such as Crofer 22 APU, ZMG 232 or E-BRITE [6–11]. Due to their high chromium contents (22 wt.% or more) the steels possess the required long-term oxidation resistance [8–13] and a coefficient of thermal expansion (CTE) similar to that of the ceramic parts of the SOFC, especially the anode substrate [8–13].

Lowering the SOFC operation temperature for instance to 600 °C would have a number of advantages such as reducing the interaction of the interconnect with cathode and anode side contact materials [11–13], reducing the formation of deleterious volatile Cr species [14] and it potentially offers the possibility to obtain higher cell efficiencies provided that suitable electrolyte and electrode materials prevail. Lower operation temperatures would also impart less stringent requirements to the CTE mismatch and are expected to lower the oxidation rates of the ferritic steels which would thus allow reducing the thickness of the interconnect from a few millimeters to a few tenths of a millimeter thereby reducing stack weight and materials cost.

The less stringent requirements in respect to CTE and oxidation behavior would therefore extend the metallic materials which might be potentially suitable for construction materials of SOFC interconnects. Examples of such materials are commercially available ferritic steels with lower Cr contents of 16–20% such as 1.4016/AISI 430; 1.4510/AISI 439 or 1.4509/AISI 441. The lower Cr contents make these steels less prone to embrittlement by σ-FeCr phase formation than the above mentioned high-Cr

* Corresponding authors. Tel.: +49 2461 612817; fax: +49 2461 613699.
E-mail addresses: l.niewolak@fz-juelich.de (L. Niewolak), j.quadakkers@fz-juelich.de (W.J. Quadakkers).

0378-7753/$ – see front matter © 2010 Elsevier B.V. All rights reserved.
doi:10.1016/j.jpowsour.2010.06.007

Table 1
Chemical compositions of the studied materials (determined by ICP-OES).

Steel type (DIN spec.)	FZJ batch	Thickness in mm	Chemical composition wt.%									
			Fe	Cr	Ni	Mn	Mo	Nb	Si	Al	Ti	La
1.4016	LKN	0.1	Bal.	16	0.22	0.44	0.02	<0.01	0.3	<0.01	<0.01	–
	LFF	0.4	Bal.	16.2	0.24	0.38	–	–	0.38	–	–	–
	LFH	1	Bal.	16.3	0.25	0.31	0.02	0.5	0.25	<0.01	<0.01	–
1.4509	LKA	0.5	Bal.	17.4	0.24	0.46	0.01	1.3	0.12	0.02	0.09	–
	LKD	2	Bal.	17.3	0.17	0.43	0.02	0.42	0.35	0.02	0.12	–
1.4520	LLB	0.4	Bal.	17.7	0.19	0.23	0.02	0.02	0.27	0.01	0.34	–
1.4521	LKY	1.8	Bal.	17.4	0.13	0.23	1.6	0.6	0.41	0.03	0.17	–
1.4760[a]	LLS	0.2	Bal.	22.9	<0.01	0.45	–	–	0.02	0.005	0.07	0.13
	LLW	1	Bal.	22.8	0.16	0.45	<0.01	<0.01	0.1	0.13	0.08	0.07
	LML	1.5	Bal.	22.7	<0.01	0.42	–	–	0.01	0.01	0.07	0.1
1.4404	LKM	0.1	Bal.	17.4	11.6	1.4	1.8	<0.01	0.42	<0.01	<0.01	–
	LKK	0.2	Bal.	17.3	11.5	1.5	2	<0.01	0.5	<0.01	0.03	–
	LKG	2	Bal.	17.4	11.1	1.4	2	<0.01	0.38	<0.01	<0.01	–
1.4845	LKZ	1	Bal.	24.2	19.1	0.85	0.23	–	0.37	–	0.03	–

[a] The steel 1.4760 exists in two variants: manufactured by conventional melting, using Al and Si addition for de-oxidation and manufactured by vacuum induction melting, thus containing lower amounts of Al and Si.

steels. They also possess better workability/formability which is advantageous when considering various cost-effective interconnect shaping methods such as stamping, pressing or milling [15]. Depending on the actually used stack design even austenitic steels could, in spite of their higher CTE, be considered as interconnect material for SOFC's operating at 600 °C. These materials would have significant advantages over ferritic steels because of their higher room temperature ductility and higher creep resistance at the operating temperatures.

In the frame of the European project SOFC600 [16] the potential suitability of a number of commercially available ferritic and austenitic steels for application in SOFC's with an operating temperature of 600 °C was investigated. This paper presents the results of these studies whereby main emphasis was put on the oxidation behavior and the microstructural stability during exposure at 600 °C in simulated SOFC service environments. Thereby not only the effect of steel composition but also the effect of component thickness (ranging from a few millimeters to a few tenths of a millimeter) was taken into account.

2. Experimental

The chemical compositions of the studied alloys determined by ICP-OES and the microstructures characterized by optical metallography are shown in Table 1 and Figs. 1 and 2, respectively. The studies included five ferritic steel compositions with Cr contents varying between 16 and 22%. All these steels prevailed in form of sheets, some of them with different thickness. The latter was also the case for the austenitic steel 1.4404, whereas the 25%Cr austenitic steel 1.4845 only prevailed as sheet with a thickness of 1 mm.

Most of the ferritic steels exhibited a recrystallized microstructure consisting of equiaxed ferrite grains, in some cases with precipitates of Ti-rich carbonitrides (Fig. 3b). One exception was the 1.5 mm batch of steel 1.4760 (designation LML) which was not fully recrystallized and showed a slight texture in rolling direction (Fig. 1). The austenitic materials possessed similar grain size exhibiting the well-known annealing twins. The microstructure of steel 1.4845 (batch LKZ) additionally contained some carbide stringers ($M_{23}C_6$) aligned parallel the rolling direction (Fig. 2).

For the oxidation tests, samples with nominal dimensions of 10 mm × 20 mm were cut from the prevailing plates. All samples made from plates with a thickness of more than 0.2 mm ("thick" materials) were subsequently ground with SiC abrasive papers down to 1200 grit surface finish. Samples of the plates with a thickness of 0.2 mm or less ("thin" materials) were used in the as-received surface conditions. Application of the standard surface preparation route used for the "thick" materials was considered to be impractical for the "thin" materials because grinding may significantly reduce specimen thickness and impart substantial plastic deformation thereby altering the exact specimen shape. The materials were tested in simulated SOFC service environments at 600 °C during discontinuous oxidation test up to a total exposure time of 1000 h using 100 h cycles. After each cycle the specimens were cooled to room temperature and gravimetrically analyzed using a microbalance (Sartorius Expert LE225D) with an absolute accuracy of 0.1 mg. For each test duplicate specimens were used. Laboratory air was chosen to simulate the cathode side environment of the SOFC. As simulating anode side service environments, the following atmospheres were used:

- Ar–4%H_2–2%H_2O, simulating the environment for the case that hydrogen is used as fuel.
- N_2–4%H_2–18.5%H_2O–4%CO–21%CO_2, simulating the environment for the case that reformed gasoline is used as fuel, assuming an 80% fuel utilization.

After exposure the surface scales formed were analyzed by optical microscopy (OM-*Leica MEF4*), scanning electron microscopy with energy dispersive X-ray spectroscopy (SEM/EDX-Leo 440/Oxford Instruments Inca), scanning electron microscopy with electron backscattered diffraction (SEM/EBSD-Leo1550, hkl Channel 5), plasma sputtered neutrals mass spectrometry (SNMS-INA 3) and X-ray diffraction (XRD-*X8 Advance*, *Bruker*). For cross-section analyses the specimens were mounted in epoxy resin. Before mounting the specimens were PVD coated with an approximately 20 nm thick Au layer and subsequently a Ni-layer with a thickness of approximately 200 μm using electroplating was applied. The Ni-layer mechanically supports the oxide scale during further metallographic specimen preparation and additionally improves contrast between oxide and mounting material during SEM or OM characterization.

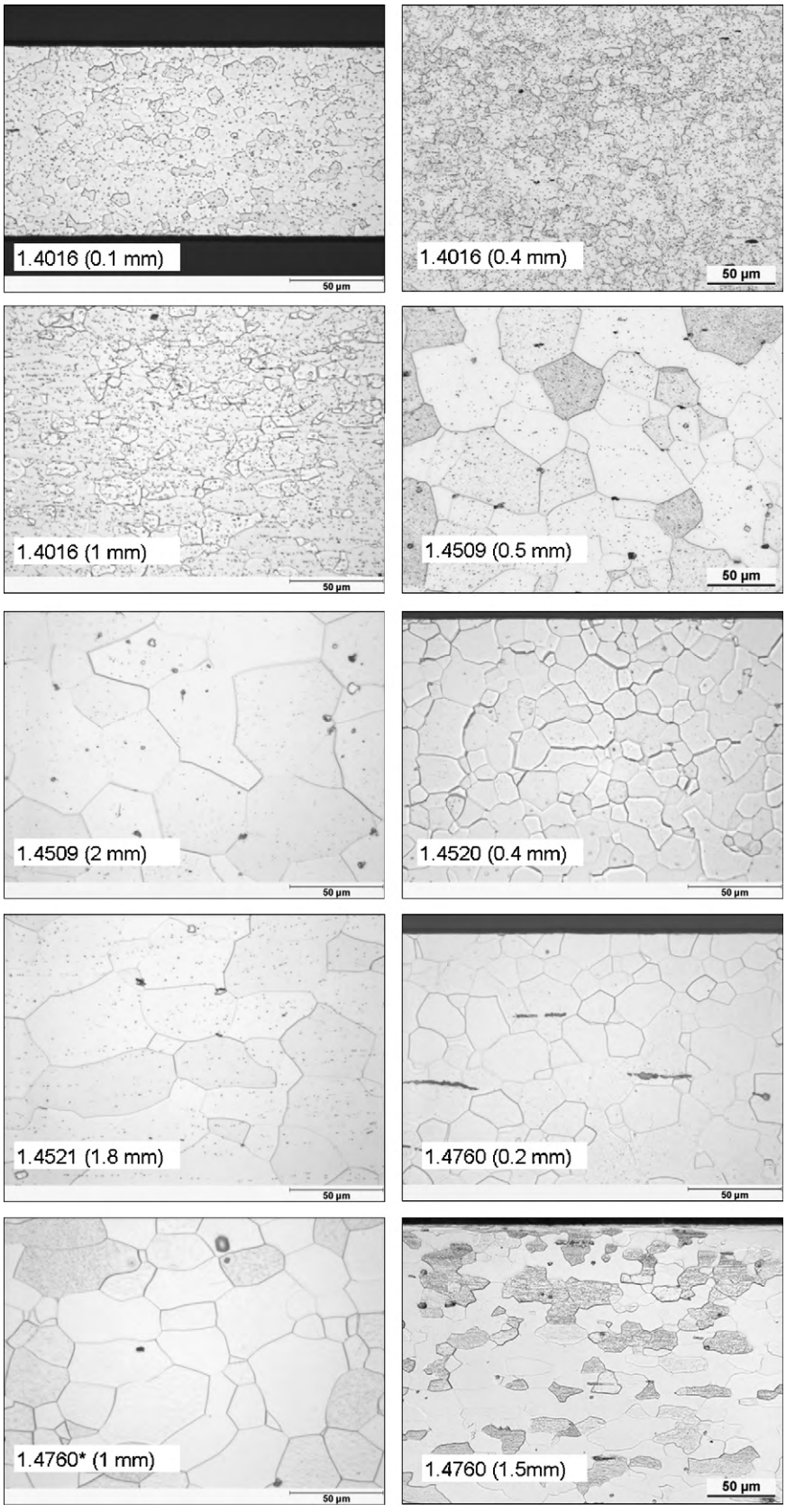

Fig. 1. Microstructures of the studied ferritic steels in the as-received condition (optical metallography, samples etched with VA-agent).

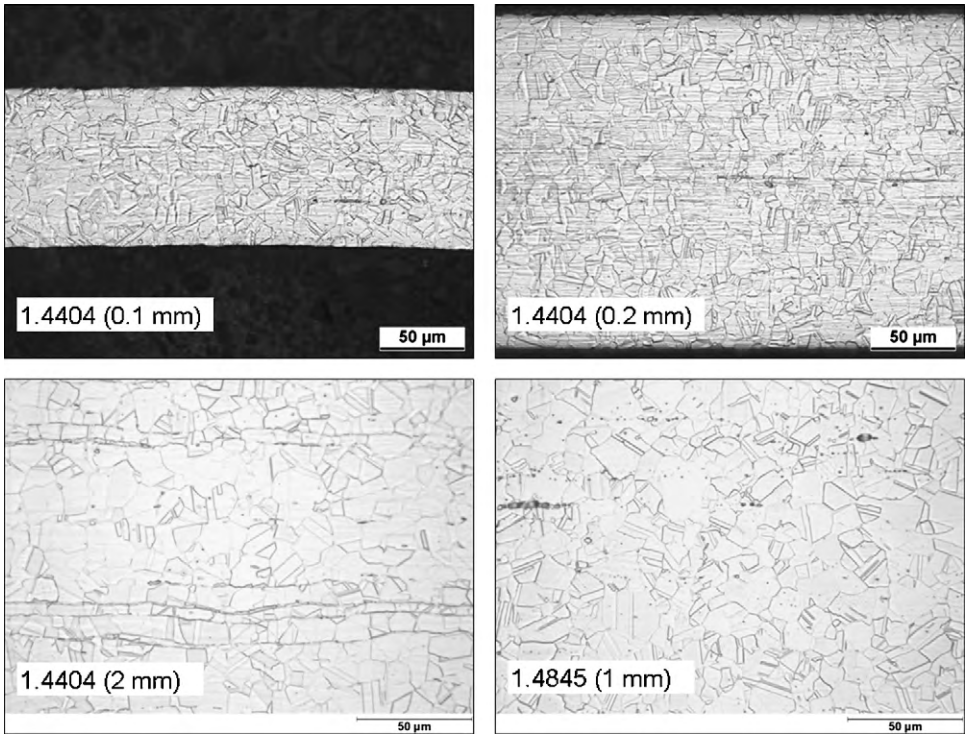

Fig. 2. Microstructures of the studied austenitic steels in the as-received condition (optical metallography, samples etched with VA-agent).

3. Results and discussion

3.1. Oxidation behavior in air

Fig. 3 summarizes the mass change data of the studied alloys after 1000 h exposure at 600 °C. In all cases very small mass changes in the range 0.1 mg/cm^{-2} were found indicating excellent oxidation resistance of the studied materials up to the maximum exposure time of 1000 h. Because the measured weight changes were close to the accuracy level of the gravimetric measurements, minor negative weight changes observed in a few cases are due to the accuracy/reproducibility of the measurement rather than to substantial spallation of the oxide scales. No clear correlation between measured mass changes and alloy Cr content was observed. This is in agreement with previous observations [17] showing that for steels which possess a sufficiently high chromium content to form a protective chromia based surface scale, the exact oxidation rates are substantially affected by presence of steel impurities and common minor alloying additions such as Mn, Si, Al, Ti rather than the exact Cr content [7].

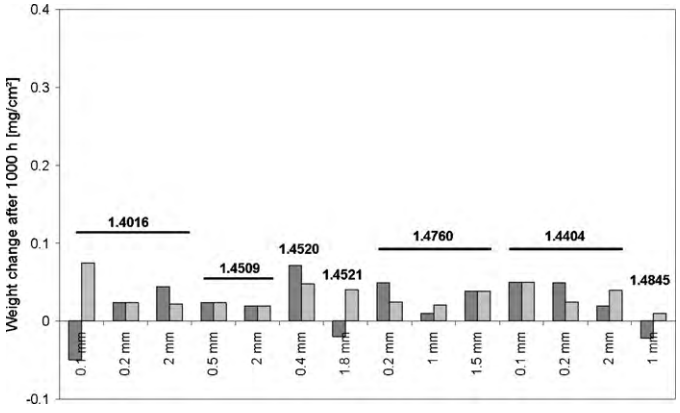

Fig. 3. Weight changes of the studied materials after 1000 h oxidation at 600 °C in air. For details on surface condition, see Section 2.

The very small mass changes are confirmed by the metallographic cross-sections presented for selected materials in Fig. 4, showing extremely thin surface oxide scales formed during the 1000 h exposure. Fig. 5 shows typical surface morphologies of the oxide scales formed on a selected austenitic and ferritic material. The scales consisted mainly of two phases, i.e. small globular Cr_2O_3 grains and larger polyhedral spinel $(Cr,Mn)_3O_4$ grains. The latter are formed due to the frequently described, strong surface enrichment of the minor alloying addition Mn [5–9] present in all studied steels. Existence of both oxide types was confirmed by XRD measurements (not presented in the paper).

SEM/EDX examinations of metallographic cross-sections (Fig. 4) confirmed that the oxide scales formed on all investigated steels had a thickness of less than 1 µm. Examples of typical SNMS profiles of two selected steels are shown in Figs. 6 and 7. It is apparent that in the ferritic as well as the austenitic steel the minor alloying elements Mn, Si, Ti tend to be enriched in the oxide scale (Mn) or near the oxide/metal interface (Si,Ti). As a result of the preferential oxidation of these alloying elements, a subsurface depletion zone was generally formed. This effect was more pronounced in the austenitic than in the ferritic steels due to the slower diffusivity of most alloying elements in the austenite than in the ferrite lattice [18]. The lower diffusivity in austenite also leads to formation of a more pronounced Cr-depletion zone beneath the surface oxide scale than in the ferritic steels (compare Figs. 6 and 7). Important to note that Si, although enriched in/beneath the oxide sale, showed hardly any depletion profile, confirming the high diffusivity of this element in the alloy matrix. The mentioned sub-scale depletion effects did in none of the studied cases result in a deterioration of the protective chromia base surface scales.

3.2. Oxidation behavior in simulated anode gases

Figs. 8 and 9 show the measured weight changes of the studied steels after 1000 h exposure in both types of simulated anode

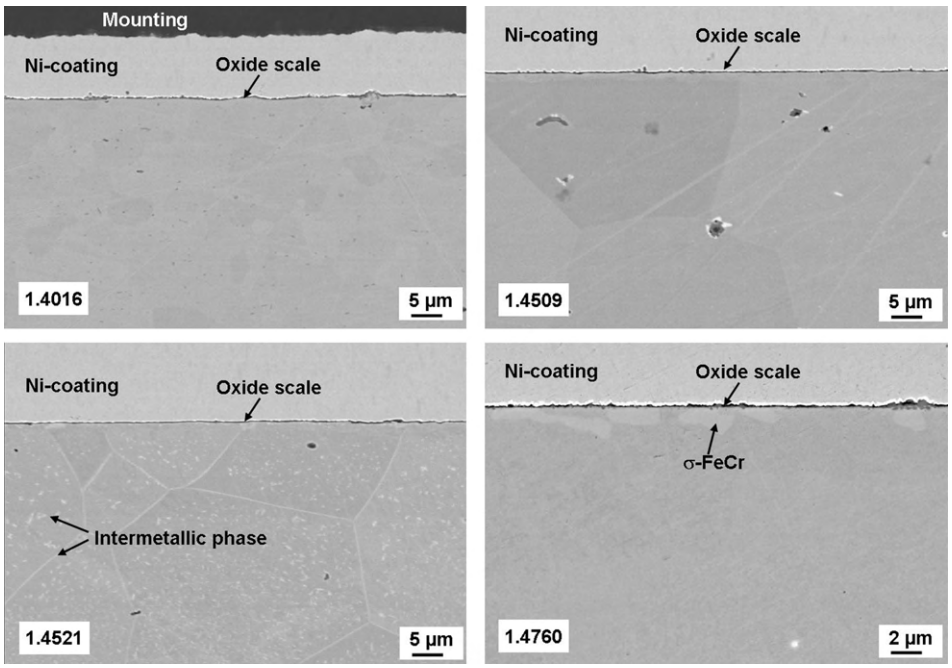

Fig. 4. SEM/BSE images showing cross-sections of oxide scales formed on selected specimens oxidized for 1000 h at 600 °C in air. 1.4016 (0.4 mm), 1.4509 (0.5 mm), 1.4521 (1.8 mm), 1.4760 (1.5 mm). All samples were ground down to 1200 grit surface finish prior to oxidation.

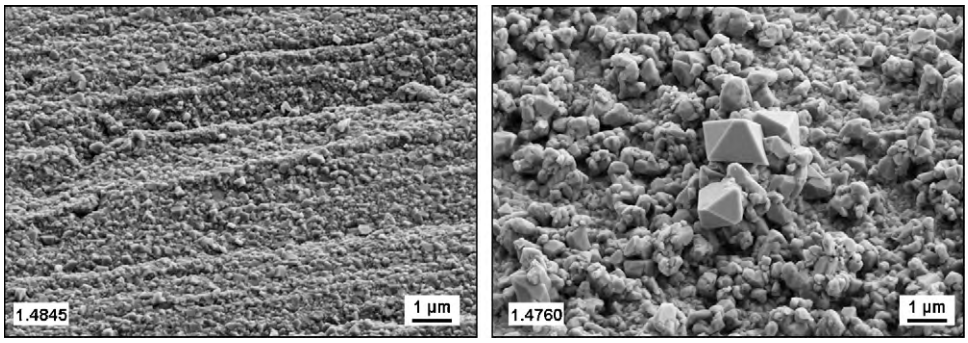

Fig. 5. SEM/SE surface morphology of oxide scales formed on selected specimens oxidized for 1000 h at 600 °C in air. 1.4845 (1 mm), 1.4760 (1.5 mm). All samples were ground down to 1200 grit surface finish prior to oxidation.

gases. Most of the tested specimens exhibited low weight changes which are in a similar range as those observed after the air exposure. However, much higher values were observed for the thin specimens of steels 1.4016, 1.4404 and 1.4760. The weight changes of these materials reached values in the range 0.66–2.4 mg cm^{-2} in the Ar–4%H_2–2%H_2O atmosphere and in the range 0.37–2.94 mg cm^{-2} in the N_2–4%H_2–18.5%H_2O–4%CO–21%CO_2 gas. It is important to note that in the latter, high water vapour containing atmosphere

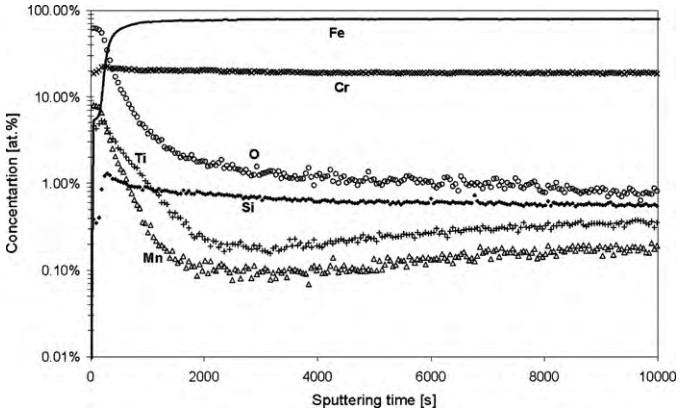

Fig. 6. SNMS depth profile of the ferritic steel 1.4520 (0.4 mm thickness) after 1000 h exposure at 600 °C in air (1200 grit surface treatment prior to exposure).

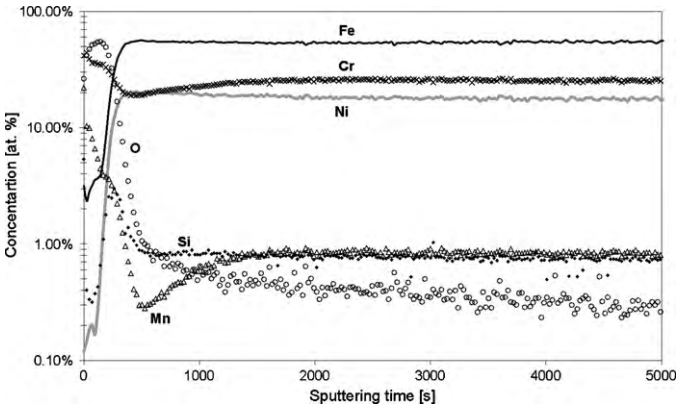

Fig. 7. SNMS depth profile of the austenitic steel 1.4845 (1 mm thickness) after 1000 h exposure at 600 °C in air (1200 grit surface treatment prior to exposure).

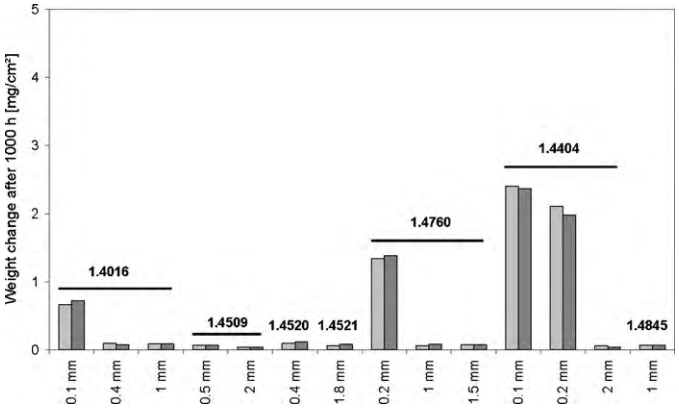

Fig. 8. Weight change of studied materials after 1000 h oxidation at 600 °C in Ar–4%H_2–2%H_2O. For details on surface condition prior to exposure, see Section 2.

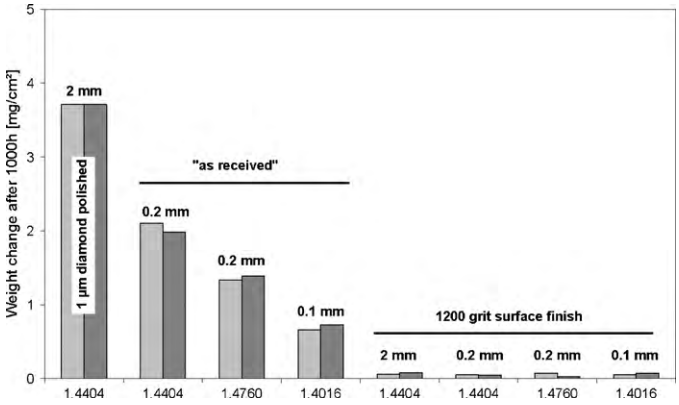

Fig. 10. Weight change for selected specimens after 1000 h oxidation at 600 °C in Ar–4%H_2–2%H_2O showing effect of surface treatment on oxidation behavior.

the 1 mm thick samples of the 16%Cr ferritic steel 1.4016 show similarly high weight changes as the 0.1 mm one, i.e. in the range 0.58–1 mg cm^{-2}.

These high oxidation rates observed for a number of specimens in the simulated anode gases might be related to the specific chemical compositions of the respective steels. However, comparison of the behavior found for the "thick" and "thin" materials of the various steels illustrates that the high oxidation rates also depend on the form in which the material prevailed, i.e. thinner specimens of a given material tended to exhibit higher oxidation rates than the corresponding thicker ones. In principal this finding might have a similar reason as described by Huczkowski et al. [19] and more recently by Zurek et al. [20] showing that chromia growth rates intrinsically tend to be higher on thin than on thick specimens. However, this finding seems not to be applicable for the thickness dependence found in the prevailing study because the higher weight changes of the "thin" specimens are not caused by higher growth rates of the formed chromia based scales but by a change from protective chromia base scale formation on the thick specimens towards formation of rapidly growing Fe-rich oxide scales on the thin ones (Fig. 12).

These differences in the tendency to protective chromia scale formation on thick and thin specimens might be affected by the used surface treatment and/or the prevailing alloy microstructure. To check whether one of these effects could be responsible for the observed differences in behavior between "thick" and "thin" materials, a second series of tests was carried out in which "thin" specimens (thickness equal or less than 0.4 mm) of the alloys 1.4404, 1.4016 and 1.4760 were subjected to a 1200 grit surface finish whereas "thick" ones (equal or thicker than 1 mm) were polished down to a 1 μm surface finish using diamond paste. The mass changes and metallographic cross-sections of these specimens after 1000 h exposure in Ar–4%H_2–2%H_2O are shown in Fig. 10. The results clearly show that the change from a protective chromia base surface scale to a more rapidly growing Fe-base oxide scale is correlated with the specimen surface treatment, irrespective of the specimen thickness. The mirror like, 1 μm diamond polishing appears to have a detrimental effect on the formation of a chromia based surface scale, whereas the 1200 grit grinding promotes protective chromia scale formation.

An important finding was that the oxidation kinetics of the 1 μm polished specimens showing formation of Fe-rich oxide scales, substantially differed between austenitic and ferritic materials (Fig. 11). Whereas the weight change curve for the polished austenitic steel 1.4404 shows a close to parabolic time dependence of the scale thickness, the weight change of the polished specimen of the ferritic steels, e.g. 1.4016, only shows a rapid weight increase during the first 100 h of oxidation (Fig. 11). After that time the weight change hardly increases and remains virtually constant during the further 900 h of oxidation.

Detailed microstructural analyses (Fig. 12a) showed that the oxide scales formed on polished specimens of the austenitic steel 1.4404 consisted of an outer layer composed mainly of iron oxide (Fe_3O_4) and an inner layer mainly containing Cr-rich oxide. The inner part of the oxide scale is relatively non-uniform and reflects features of the original alloy microstructure as it consists of inter-

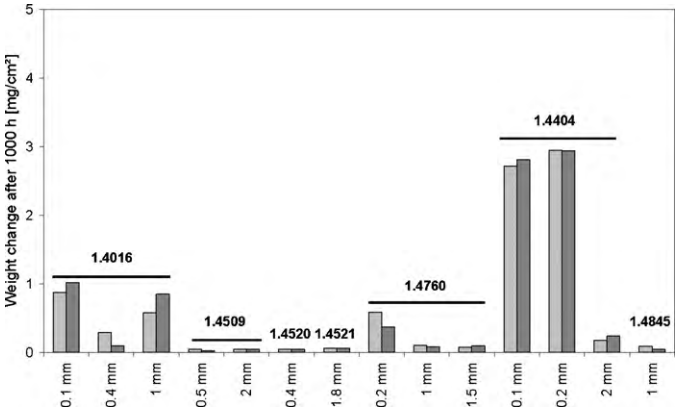

Fig. 9. Weight change of studied materials after 1000 h oxidation at 600 °C in N_2–4%H_2–18.5%H_2O–4%CO–21%CO_2. For details on surface condition prior to exposure, see Section 2.

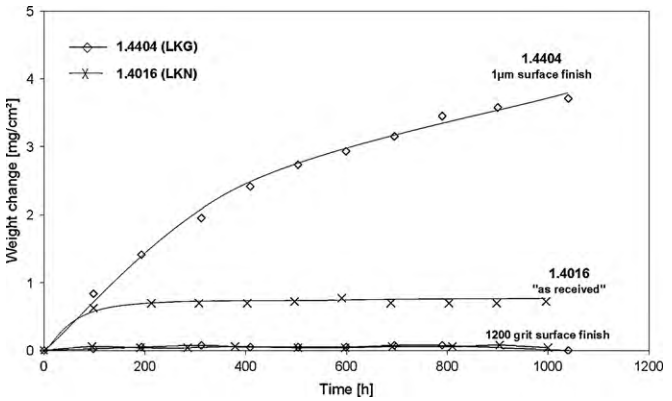

Fig. 11. Effect of surface finish on weight changes for austenitic steel 1.4404—(2 mm thick) and ferritic steel 1.4016 (0.1 mm thick) during 1000 h oxidation at 600 °C in Ar–4%H_2–2%H_2O.

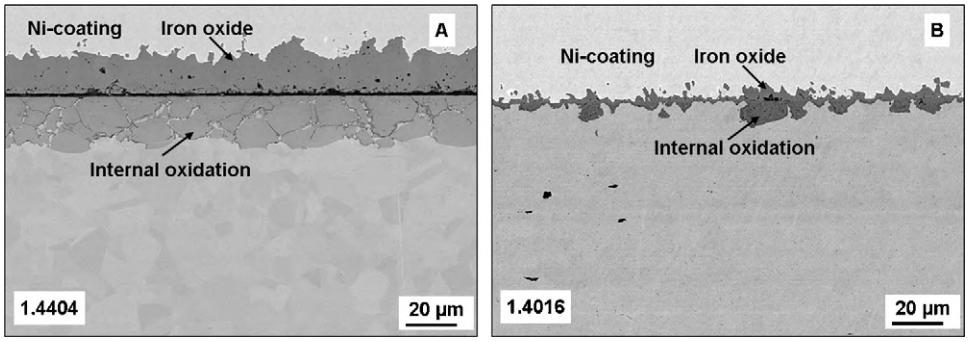

Fig. 12. SEM/BSE images of cross-sections showing Fe-rich oxide formation on selected ferritic and austenitic steel specimens after 1000 h exposure at 600 °C in Ar–4%H_2–2%H_2O. 1.4404 (2 mm thick, 1 μm surface finish prior to exposure); 1.4016 (0.4 mm thick, "as-received").

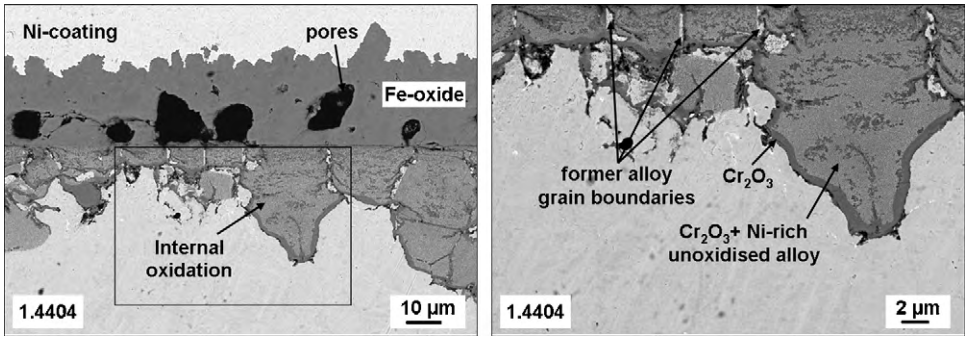

Fig. 13. SEM/BSE images of cross-sections showing oxide scale formed on austenitic steel 1.4404 (0.1 mm thick, "as-received") after 1000 h exposure at 600 °C in N_2–4%H_2–18.5%H_2O–4%CO–21%CO_2.

nally oxidized alloy grains. The grain boundaries exhibit adjacent layers of protective Cr-rich oxide and non-oxidized (Fe,Ni)-rich metal (Fig. 13). The oxidized grains contain very fine precipitates of chromium oxide separated by Cr depleted alloy regions. In contrast, the oxide scales formed on large areas of the polished ferritic steel surface are thin and consist of a layer composed mainly of Cr_2O_3 and $MnCr_2O_4$ (Fig. 12b). Only local formation of non-protective, Fe-rich oxide scale can be seen. In these places the inner part of the oxide scale is relatively non-uniform and seems to reflect microstructural features of the alloy. A detailed EBSD investigation (Fig. 14) showed that the inner part of the areas with non-protective oxide is mostly restricted to single ferrite grains which are completely internally oxidized and are separated by other grains which only exhibit formation of a protective chromia-rich surface layer. Comparison with Fig. 13 shows that the microstructure of the internal part of the non-protective oxide scale on ferritic materials differs from that on austenitic ones. Two reasons may be responsible for this difference:

- Because Cr diffusion in the austenitic alloy matrix is slower than that in the ferritic one, the enhanced attack in case of the latter material is less likely, and thus occurs only locally, whereas a homogenous attack occurs in case of the austenite.
- The first stage of the non-protective scale formation is internal oxidation of Cr in the alloy grains. After Cr in the alloy matrix has been virtually completely depleted by this process, the Fe in the surrounding matrix starts to oxidize. In case of the ferrite this result in an "oxide crater" consisting of a Fe- and Cr-containing oxide mixture. In case of the austenite, however, the Ni remaining after the Cr and Fe have been completely oxidized, cannot be transformed into oxide because the oxygen partial pressure in the used test environment is lower than the dissociation pressure of NiO. Therefore, remnants of pure Ni are found in the inner oxide scale (Fig. 13).

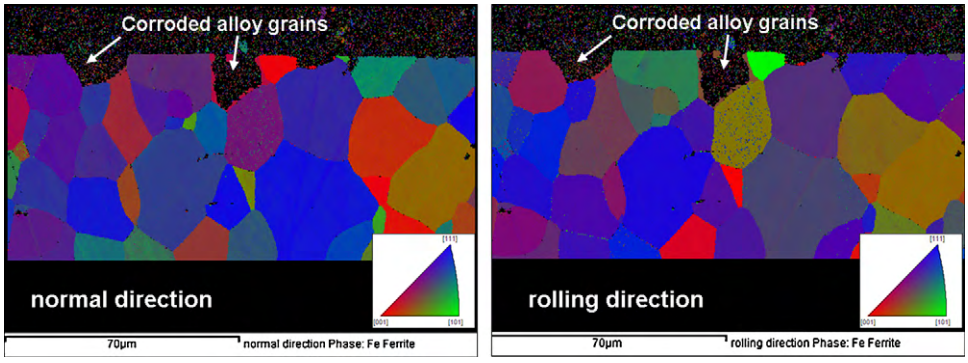

Fig. 14. SEM/EBSD mapping on cross-section of oxide scale formed on steel 1.4760 (0.2 mm thick, 4000 grit surface finish prior to exposure) oxidized for 1000 h at 600 °C in N_2–4%H_2–18.5%H_2O–4%CO–21%CO_2.

3.3. Parameters affecting protective chromia surface scale formation

The oxidation rate of low-Cr FeCr-base alloys in oxygen or air is known to slowly decrease if the Cr content is increased. This is related to increasing amounts of more protective oxides, chromia and/or Cr-rich Fe/Cr spinel, which are being incorporated into the Fe-rich surface scale [17]. If a critical Cr content is exceeded, the alloy forms an external chromia base scale resulting in a growth rate which is up to five orders of magnitude smaller than that of pure Fe or low-Cr alloys [17]. Generally it can be said, that the critical Cr concentration is increased by high oxygen solubility and diffusivity in the alloy and/or low Cr diffusivity. Also a high ratio between oxidation rate constant and Cr diffusivity in the alloy promotes non-protective scale formation [17]. The exact concentration of chromium needed for external chromia formation is affected by numerous factors such as temperature, alloy grain size, alloy impurities, minor alloying additions and composition of the oxidizing atmosphere. In many oxidation studies it has been found, that the critical Cr content for obtaining protective external chromia formation is also affected by the specimen/component surface treatment (see e.g. [21]). Machining or grinding introduces cold work in the surface-near region of the sample resulting in a high dislocation density. These "imperfections" are known to be preferential paths for diffusion of Cr from the bulk alloy towards the surface thus promoting the formation of a protective chromia base surface scale [21]. Enhanced Cr diffusion towards the surface can also be obtained by a small grain size of the starting materials thus increasing the density of alloy grain boundaries which act as rapid diffusion paths for chromium. This explains the results shown in Figs. 8 and 10.

A sensitivity of the oxidation rate on the actual surface treatment (Fig. 1) could not be found during air exposure for the alloys studied. In this atmosphere protective chromia base scale formation was found in all studied cases irrespective of the surface condition of the studied test specimens. Apparently the critical chromium content for protective chromia scale formation in air is substantially lower than in the two simulated anode gases. Based on numerous investigations (see e.g. [22–24]) this is very likely related to the presence of water vapour in the anode side environments. Already in early studies [25,26] it was shown that presence of water vapour (in oxidizing atmospheres) increases the critical Cr content for formation of protective chromia scales which means that for a given alloy with an intermediate Cr content protective chromia scale formation may occur during air or oxygen exposure, whereas poorly protective Fe-base scales are being formed in wet gases. The major mechanisms which have been proposed in literature to explain this deleterious effect of water vapour are summarised in [23–28].

The formation of the rapidly growing Fe-base oxides in the wet gases, of course, only occurs if the equilibrium oxygen partial pressure of the gas is higher than the dissociation pressure of Fe oxide. In an Ar–H_2–H_2O gas this corresponds to a H_2/H_2O ratio near to one [28]. The Ar–4%H_2–2%H_2O gas used in the present study is thus a "borderline" case for formation of Fe-oxide scales whereas in the second simulated anode gas, N_2–4%H_2–18.5%H_2O–4%CO–21%CO_2, the Fe oxide can, from the viewpoint of thermodynamic driving force, easily form. In the latter gas, the occurrence of the non-protective scale formation is more likely to occur than in the used Ar–H_2–H_2O mixture not only because of the higher H_2O/H_2 ratio, but also due to the fact that presence of CO_2 and/or CO has also been shown to adversely affect protective chromia scale formation. This explains the different results obtained for steel 1.4016 in the two simulated anode gases (Figs. 8 and 9).

During oxidation at 600 °C in air protective chromia base scale formation was observed for all the tested alloys, including the coarse grained "thin" materials of alloys 1.4404, 1.4016 and 1.4760 in the as-received state. This means that the critical Cr content for all the alloys, irrespective of the surface treatment and/or microstructure, at 600 °C in laboratory air is less than 16 mass.%. In the water vapour containing simulated anode gases the critical Cr content for coarse grained, polished ferritic steels at this temperature is even higher than 22% whereas in case of ground material the value is close to 16%. As already mentioned in Section 3.3 the mentioned critical Cr concentrations should only be considered as approximate values because they are known to be affected, e.g. by alloy impurities and minor alloying additions [17,27,29].

3.4. Microstructural stability of the steels during 600 °C exposure

The as-received microstructure of the steels may change during high temperature exposure not only as a result of internal and/or external oxidation process, but also just as a result of the thermal treatment at 600 °C. Most commonly observed changes are an alteration in grain size, formation of new precipitates and/or coarsening of existing precipitates. A major microstructural change which is expected to occur during a 600 °C treatment of high Cr steels, especially ferritic steels, is the formation of the intermetallic σ-FeCr phase, which is known to adversely affect the room temperature ductility and thus formability of the steels [30,31]. Literature data [32,33] and existing phase diagrams [34] indicate that in a binary Fe–Cr alloy annealed at 600 °C the critical Cr concentration needed for σ-FeCr formation can be 16–26 mass%. However, the presence of further alloying elements is known to substantially change the critical Cr concentration above which σ-phase formation occurs. Based on the existing ternary phase diagrams [35], alloying elements which promote σ-phase formation are e.g. Mo and Si, whereas e.g. Al, Ti and Ni in minor amounts, should have hardly any effect or may even suppress σ-phase formation. It should further be mentioned that, additions of Mo, W and/or Nb can promote formation of other intermetallic phases such as Laves phase Me_2X where Me = (Cr, Fe) and X = (Mo, W, Nb, Ta, Si) and/or τ_1- or χ-phase [35].

Among all investigated ferritic 16–22% Cr alloys only the steels 1.4521 and 1.4760 clearly showed formation of intermetallic precipitates after exposure at 600 °C. Fig. 4 shows an SEM/BSE image of both steels after 1000 h oxidation at 600 °C in air. In steel 1.4760 the σ-FeCr phase is formed only near the specimen surface. The chemical analyses of the σ-FeCr grains measured with SEM/EDX showed that the phase only consists of iron (57 at.%) and chromium (43 at.%). No other elements were detected in the σ-FeCr grains. The preferential nucleation of σ-phase near the surface was also observed by Hammer et al. [36] when studying the behavior of 26% Cr/1% Mo ferritic steel at 700 °C in various SOFC relevant service environments. It is presently not known, whether the early σ-phase formation near the surface is related to preferential nucleation conditions or whether, e.g. the σ-phase is stabilized by minor amounts of oxygen and/or other species present in the service environments. The latter might be derived from the results of Hammer et al. [36] who found for the 26% Cr/1% Mo (wt.%) steel at 700 °C σ-phase nucleation to differ in anode and cathode side gases. The authors found σ-phase formation at 700 °C only in the ferritic 26% Cr and 1% Mo steel, not in a steel containing 22% Cr. In the present study thick material of the ferritic steel (1.4760; ground 1200 grit) formed σ-phase during exposure in air, however not in anode gas. The thin material of this steel in as-received condition did not form σ-phase at all. The thicker material (ground 1200 grit) of the batch of this alloy which contained slightly higher amounts of Al and Si (batch LLW) formed σ-phase during air exposure, but in smaller amounts than the high purity batch (LML).

In the steel 1.4521 formation of another intermetallic phase was observed. This phase did not precipitate in form of coarse, separated grains but as needle shaped precipitates within the ferrite grains and in form of a thin layer at the alloy grain boundaries (Fig. 4). SEM/EDX examinations showed that these contained significant amounts of molybdenum and silicon and are characterized by the following chemical composition (given in at.%): Fe–52%, Mo–18%, Cr–17%, Si–8%, Nb–3%, Ti–2%. Due to the small size of the precipitates (350–400 nm) the quantitative EDX analysis has to be treated with some caution, however, based on literature data [30–35] and the above EDX results the phase may be a Laves phase $(Fe,Cr)_2(Mo,Si,Nb)$ or τ_1-phase. The other investigated lower Cr ferritic steels did, after the 600 °C exposure, not show evidence of intermetallic phase formation.

4. Conclusions

The presented investigations have revealed excellent oxidation resistance during air exposure at 600 °C up to 1000 h for a number of selected commercially available ferritic and austenitic steels with Cr contents ranging from 16 to 25 mass%. The materials formed very slowly growing, double layered surface oxide scales mainly consisting of an inner chromia layer and an outer Cr/Mn-base spinel phase, irrespective of the exact steel Cr content. Although the oxidation behavior was affected by presence of different types and concentration of minor alloying additions, this scale formation was observed for all studied materials irrespective of the steel grain size or detailed specimen surface treatment.

During exposure in two simulated anode gases the type and the growth rates of the surface oxide scales strongly depended on the exact steel composition as well as on the steel microstructure and specimen surface treatment. The studied ferritic steel (1.4016) with less than 17% Cr showed in these gases a large tendency to the formation of poorly protective Fe-base oxide scales, irrespective of surface treatment. This type of oxide formation was also observed in ferritic and austenitic steels with higher Cr contents, however for these materials the undesired effect only occurred for steels with a large grain size and if no surface cold work, e.g. by grinding, was introduced to the specimen surface. On coarse grained, diamond polished materials the tendency to formation of poorly protective oxide scales was found for nearly all studied alloys, with the exception of the studied austenitic steel 1.4845 with a Cr content as high as 25%.

The larger tendency to formation of poorly protective Fe-base oxide scales in the anode side gases than in air, can be explained by the frequently described mechanisms explaining the suppression of protective chromia scale formation due to presence of high amounts of water vapor (with or without CO/CO_2) in the service environment.

Higher Cr contents for obtaining better oxidation resistance and/or additions of Mo for improving mechanical properties have as major drawback that they enhance the tendency to precipitation of embritteling intermetallic phases such as σ-phase, Laves phase or τ_1-phase. High ductility/formability at room temperature in combination with high oxidation resistance at 600 °C might thus require the use of fine grained steel with a moderate Cr content.

Acknowledgement

The authors are grateful for financial support from the European Commission under contract No. SES6-2006-020089 (project SOFC600).

References

[1] W.R. Grove, Philosophical Magazine 21 (1842) 417–420.
[2] E. Baur, H. Preis, Zeitschrift für Elektrochemie 43 (1937) 727–732.
[3] O. Yamamoto, Y. Takeda, R. Kanno, M. Noda, Solid State Ionics 22 (1987) 241–246.
[4] J. Divisek, L.G.J. de Haart, P. Holtappels, T. Lennartz, W. Malléner, U. Stimming, K. Wippermann, Journal of Power Sources 49 (1994) 257–270.
[5] P. Kofstad, R. Bredesen, Solid State Ionics 52 (1992) 69–75.
[6] W.J. Quadakkers, H. Greiner, W. Köck, in: U. Bossel (Ed.), Proceedings 1st European Solid Oxide Fuel Cell Forum 2, Baden, Switzerland, 1994, pp. 525–541.
[7] W.J. Quadakkers, J. Piron-Abellan, V. Shemet, L. Singheiser, Materials at High Temperatures 20 (2003) 115–127.
[8] J. Piron-Abellan, V. Shemet, F. Tietz, L. Singheiser, W.J. Quadakkers, Proceedings The Electrochemical Society 2001-16, 2001, pp. 811–819.
[9] Z. Yang, K. Scott, W. Dean, M. Paxton, J.W. Stevenson, Journal of The Electrochemical Society 150 (2003) 1188–1201.
[10] J.W. Fergus, Materials Science and Engineering A 397 (2005) 271–283.
[11] I. Antepara, I. Villarreal, L.M. Rodríguez-Martínez, N. Lecanda, U. Castro, A. Laresgoiti, Journal of Power Sources 151 (2005) 103–107.
[12] W.J. Quadakkers, H. Greiner, M. Hänsel, A. Pattanaik, A.S. Khanna, W. Malléner, Solid State Ionics 91 (1996) 55–67.
[13] S. Fontana, R. Amendola, S. Chevalier, P. Piccardo, G. Caboche, M. Viviani, R. Molins, M. Sennour, Journal of Power Sources 171 (2007) 652–662.
[14] W.J. Quadakkers, H. Greiner, W. Köck, H.P. Buchkremer, K. Hilpert, D. Stöver, Proceedings of 2nd European Solid Oxide Fuel Cell Forum, 1996, pp. 297–306.
[15] J.T. Black, R.A. Kohser, Materials and Processes in Manufacturing, John Wiley & Sons, Inc., 2008, ISBN: 9780470-05512-0.
[16] http://www.sofc600.eu/.
[17] N. Birks, G.H. Meier, F.S. Pettit, Introduction to the High-Temperature Oxidation of Metals, Cambridge University Press, 2006, ISBN: 978-0-521r-r48042-0.
[18] Zs. Tokai, K. Hennesen, H. Viefhaus, H.J. Grabke, Materials Science and Technology 16 (2000) 1129–1138.
[19] P. Huczkowski, S. Ertl, J. Piron-Abellan, N. Christiansen, T. Höfler, V. Shemet, L. Singheiser, W.J. Quadakkers, Materials at High Temperatures 22 (2005) 79–88.
[20] J. Zurek, G.H. Meier, E. Essuman, M. Hänsel, L. Singheiser, W.J. Quadakkers, Journal of Alloys and Compounds 467 (2009) 450–458.
[21] S. Leistikow, I. Wolf, H.J. Grabke, Werkstoffe und Korrosion 38 (1987) 556–562.
[22] M. Thiele, H. Teichmann, W. Schwarz, W.J. Qudakkers, H. Nickel, VGB Kraftwerkstechnik 2 (1997) 129–134.
[23] A. Galerie, S. Henry, Y. Wouters, M. Mermoux, J.P. Petit, L. Antoni, Materials at High Temperatures 22 (2005) 105–112.
[24] E. Essuman, G.H. Meier, J. Zurek, M. Hänsel, W.J. Quadakkers, Oxidation of Metals 69 (2008) 143–162.
[25] A. Rahmel, J. Tobolski, Corrosion Science 5 (1965) 333–340.
[26] C.T. Fujii, R.A. Meussner, Journal of The Electrochemical Society 111 (1964) 1215–1221.
[27] D.J. Young, High Temperature Oxidation and Corrosion of Metals, Elsevier, 2008, ISBN: 978-0-08r-r044587-8.
[28] J. Zurek, M. Michalik, L. Singheiser, W.J. Quadakkers, Materials Science Forum 522/523 (2006) 155–162.
[29] W.J. Quadakkers, J. Żurek, Oxidation in Steam and Steam/Hydrogen Environments Shreir's Corrosion, 2010, pp. 407–456, ISBN: 978-0-444r-r52787-5.
[30] A. Marucco, Materials Science and Engineering A 194 (1995) 225–233.
[31] J.O. Nilsson, P. Kangas, T. Karlsson, A. Wilson, Metallurgical and Materials Transactions A 31A (2000) 35–45.
[32] T. Ujihara, K. Osamura, Acta Materialia 448 (2000) 1629–1637.
[33] Y. Usitnovshikov, B. Pushkarev, I. Igumnov, Journal of Materials Science 37 (2002) 2031–2042.
[34] T.B. Massalski, Binary Alloy Phase Diagrams, ASM International, 1990, ISBN: 0-87170r-r404-8.
[35] P. Villars, A. Prince, H. Okamoto, Handbook of Ternary Alloy Phase Diagrams, 7 ASM International, 1995.
[36] J.E. Hammer, S.J. Laney, R.W. Jackson, K. Coyne, F.S. Pettit, G.H. Meier, Oxidation of Metals 67 (2007) 1–38.